

Impact of Space Weather on Space Assets and Satellite Launches

Julia Briden^{*}, Nicolette Clark[†], Peng Mun Siew[‡], Richard Linares[§]

Massachusetts Institute of Technology

Tzu-Wei Fang[¶]

National Oceanic and Atmospheric Administration

ABSTRACT

To analyze the impact of space weather activity on Low Earth Orbit (LEO) Resident Space Objects (RSOs), empirical, physics-based, and reduced-order atmospheric density models are compared for use in satellite deorbit prediction. In this work, the Starlink, Humanity Star, and the Freedom Drag Sail CubeSat deorbit events are predicted with the NRLMSISE-00, JB2008, Proper Orthogonal Decomposition (POD) Reduced-Order Models (ROMs) based on JB2008 and TIE-GCM, and JB2008-based Machine Learning (ML) ROM atmospheric density models. The High Precision Orbital Propagator (HPOP) is used to model each satellite's motion under the model-provided atmospheric density and a Two-Line Element (TLE)-based Ballistic Coefficient (BC) estimate. A sensitivity analysis is performed to quantify the effects of space weather inputs for the propagation of atmospheric density states. The JB2008, JB2008 PODROM, and JB2008 MLROM are propagated with the COSPAR International Reference Atmosphere (CIRA-08) reference space weather inputs as well as with true space weather indices corrupted by Gaussian noise. The NRLMSISE-00 model performed best, an expected result due to its use in the BC estimation process. As measured by RMS difference from a TLE-extrapolated reentry time, the three ROMs demonstrated similar results; the ROMs had the best performance, after the NRLMSISE-00. In addition, the MLROM results were the most robust to the use of reference space weather data, while the JB2008 was the least sensitive to space weather noise. These results illustrate the importance of space weather prediction and modeling to minimize the impact of future solar storms on RSO failure and loss of custody.

1. INTRODUCTION

Recently, fluctuations in solar and geomagnetic activity have resulted in increased Low Earth Orbit (LEO) satellite failure and the loss of custody of Resident Space Objects (RSO). With a single geomagnetic storm's ability to inhibit the majority of LEO satellite tracking activity for several days, space weather activity poses a high conjunction risk for Earth-orbiting satellites. These failures occur because these fluctuations were not modeled accurately, resulting in inaccurate atmospheric density estimates used for computing the atmospheric drag. With the number of satellites in LEO growing by over 50% in the past year and the predicted solar cycle reaching maximum activity by 2025, accurate atmospheric density estimation for a range of solar and geomagnetic conditions is essential in deorbit event prediction, satellite orbit prediction, and collision avoidance [1].

Space weather activity in the Earth's atmosphere occurs in two forms: solar activity and geomagnetic activity. Eruptions of plasma and magnetic field structures, known as coronal mass ejections (CMEs), occur in the sun's atmosphere. When charged particles from these eruptions enter the Earth's atmosphere, the atmospheric temperature rises due to Joule heating from electric fields in the ionosphere [2]. The atmospheric heating from solar activity and the transient solar wind from Earth-directed CMEs determine the level of geomagnetic activity, sometimes resulting in geomagnetic storms. One of the largest solar storms of the Space Age occurred from mid-October to early November in 2003. The storm caused temporary to permanent communications losses for the ADEOS-2, CHIPS, and Department of Defense satellites and resulted in additional complications for Global Positioning System (GPS) applications and electrical

^{*}Ph.D. Student, Department of Aeronautics and Astronautics. E-mail: jbriden@mit.edu

[†]Graduate Student, Department of Aeronautics and Astronautics. E-mail: nlclark@mit.edu

[‡]Postdoctoral Associate, Department of Aeronautics and Astronautics. E-mail: siewpm@mit.edu

[§]Associate Professor, Department of Aeronautics and Astronautics. E-mail: linaresr@mit.edu

[¶]Space Scientist, NOAA Space Weather Prediction Center. E-mail: tzu-wei.fang@noaa.gov

power systems [3]. Atmospheric density is influenced by time-dependent changes in solar and geomagnetic activity, as well as altitude-dependent changes in thermal activity. To capture and predict these fluctuations for LEO satellite orbit tracking, highly-accurate and efficient atmospheric density models must be employed.

In practice, atmospheric density models include empirical models, such as NRLMSISE-00 [4], JB2008 [5], and DTM-2013 [6], and physics-based models, including the Global Ionosphere-Thermosphere Model (GITM) [7], the coupled Whole Atmosphere Model-Ionosphere Plasmasphere Electrodynamics (WAM-IPE) model [8], and the Thermosphere-Ionosphere-Electrodynamics General Circulation Model (TIE-GCM) [9]. Empirical models are fast to evaluate, at the expense of limited accuracy, and exclude the dynamics of the atmosphere required for forecasting. Conversely, physics-based models solve the full Navier-Stokes equations for density, velocity, and temperature on a discretized grid, allowing for accurate forecasts at a high computational cost. Recent work in reduced-order modeling has represented physics-based atmospheric density models with a small set of spatial modes to improve the computational efficiency of forecasting models [10]. Additionally, data assimilation of two-line element (TLE) data and combined satellite radar and GPS tracking data into reduced-order atmospheric density models (ROMs) has significantly increased the accuracy of these models [11, 12]. While performance comparisons of these atmospheric density models have previously been conducted, a full study of the effectiveness of these models in RSO orbit prediction during significant solar and geomagnetic space weather events for satellite reentry prediction has not been explored. Due to the large variation in density with altitude, the errors in density estimates are compounded in satellite reentry prediction scenarios.

This work analyzes the accuracy of the NRLMSISE-00, JB2008, Proper Orthogonal Decomposition (POD) ROMs based on JB2008 and TIE-GCM [13, 12], and JB2008-based Machine Learning (ML) ROM atmospheric density models [14] for LEO orbit propagation during deorbit events for Starlink, Rocket Lab's Humanity Star, and drag sail CubeSats. Drag is the largest perturbation for orbit prediction, requiring an accurate ballistic coefficient (BC) to be estimated [15]. Often, the true values of the BCs for LEO RSOs are not readily available, requiring BCs to be estimated from TLE data; the BSTAR value in TLE files is only compatible with the SGP4 orbit propagator. The BC is estimated in this work by iteratively optimizing our estimate by comparing the change in semimajor axis based on TLE data to the semimajor axis change due to drag, as computed by orbit propagation [16, 17]. For the POD and MLROMs, the reduced-order thermospheric density states are predicted using the Density Estimation Toolbox (DESTO) [11]. The DESTO toolbox is available in two programming languages; Matlab ¹ and Python ². In this work, we will be mainly using the Python version of the DESTO toolbox. These states, along with estimated BCs for each satellite, are used as inputs to the orbit propagator. A sensitivity analysis is performed for each event by comparing the reentry predictions of three density models (JB2008, JB2008 PODROM, and JB2008 MLROM) using true space weather data to the predictions of the same three models using noisy space weather data. For the noisy cases, true space weather indices are corrupted using a Gaussian model developed with reference data from COSPAR International Reference Atmosphere 2008 (CIRA-08). The same three models are also run directly on the CIRA-08 reference space weather data for further comparison.

By developing a method for evaluating the prediction ability and performance of atmospheric density models for deorbit events, important preventative measures can be identified. With some of the most important space assets, along with the highest concentration of space debris residing in LEO, space weather modeling has the ability to predict and respond to future orbit determination hazards.

2. THEORY

For LEO satellites, atmospheric drag is the dominant orbital perturbation after non-spherical Earth gravitational effects. Accurate drag predictions are especially important in the context of reentry, where the drag force on a satellite may even become the single dominant perturbation as the satellite re-enters the atmosphere and encounters higher atmospheric densities. Furthermore, the atmospheric densities can vary greatly with altitude. Because of its importance at reentry altitudes, the accuracy of atmospheric drag predictions is fundamental to the quality of reentry predictions and analysis. A satellite's acceleration due to drag is expressed in the Equation 1 [18].

¹ Available at <https://github.com/davidgondelach/DESTO>

² Available at <https://github.com/pengmun/DESTOPy>

$$\vec{a}_{drag} = -\frac{1}{2} \frac{C_d A}{m} \rho v_{rel}^2 \frac{\vec{v}_{rel}}{|\vec{v}_{rel}|} \quad (1)$$

where C_d is the drag coefficient, A is the effective frontal area of the satellite, m is the satellite mass, ρ is the local mass density of the atmosphere, and \vec{v}_{rel} is the relative velocity between the satellite and surrounding atmosphere. The term $\frac{C_d A}{m}$ is often called the ballistic coefficient (BC), and is frequently estimated collectively rather than in its component parts. In order to accurately calculate the drag force on a satellite, both BC and the atmospheric density ρ must be accurately modeled. An analysis of simulating the reentry of Gravity field and steady-state Ocean Circulation Explorer (GOCE) found that both the accuracy and precision of reentry-time estimates were dominantly dependent on errors in atmospheric density and in attitude control (which affects A , and thus the BC) [19]. This paper is focused primarily on the effects on reentry simulation accuracy of using ρ computed with several different atmospheric density models. Secondly, we improved reentry simulations by incorporating empirical BC estimates using a TLE-based estimation technique developed in [16]. The unique contributions of this paper are 1) the use of Reduced-Order atmospheric density Models (ROMs) for reentry analysis, and 2) the comparison of ROM performance in reentry analysis to the performance of other existing density models.

2.1 Reduced-Order Modeling

Nonlinear and linear reduced-order modeling methods were utilized to generate fast-to-evaluate predictive models for atmospheric density. To obtain a ROM, the full state of atmospheric mass density values are reduced to a pre-specified dimension via proper orthogonal decomposition (POD) or using a convolutional neural network (CNN) autoencoder model. The process used to obtain the reduced order state for each method is described in 2.1.1 and 2.1.2, respectively. A linear dynamical model is then constructed with the reduced-order density states using Dynamic Mode Decomposition with control (DMDc). The DMDc formulation allows for the prediction of future density states with space weather indices as the input. The DMDc algorithm is outlined in 2.1.3.

2.1.1 Proper Orthogonal Decomposition

In POD, a small number of spatial modes are used to represent a high-dimensional system. This is achieved by computing the singular value decomposition of the snapshot state that contains the variation in atmospheric mass density, $\tilde{\mathbf{x}}$, for different times. The variation in atmospheric mass density is described by Equation 2.

$$\tilde{\mathbf{x}}(\mathbf{s}, t) = \mathbf{x}(\mathbf{s}, t) - \bar{\mathbf{x}}(\mathbf{s}) \quad (2)$$

where \mathbf{x} is the atmospheric mass density, $\bar{\mathbf{x}}$ is the mean value, \mathbf{s} is the spatial grid, and t is the time index. The first r principal spatial modes of $\tilde{\mathbf{x}}$ are defined by Equation 3.

$$\tilde{\mathbf{x}}(\mathbf{s}, t) \approx \sum_{i=1}^r c_i(t) \phi_i(\mathbf{s}) \quad (3)$$

where ϕ_i are the spatial modes and c_i are the time-dependent coefficients. To compute the spatial modes, a singular value decomposition is taken. The snapshot matrix, containing atmospheric mass density variations for a set of m times, can be decomposed in the form of Equation 4.

$$\mathbf{X} = [\tilde{\mathbf{x}}_1 \tilde{\mathbf{x}}_2 \dots \tilde{\mathbf{x}}_m] = \mathbf{U} \mathbf{\Sigma} \mathbf{V}^T \quad (4)$$

The spatial modes are given by the left singular vectors, or columns of \mathbf{U} . The reduced state is computed using a similarity transform for the first r POD modes:

$$\mathbf{z} = \mathbf{U}_r^{-1} \tilde{\mathbf{x}} = \mathbf{U}_r^T \tilde{\mathbf{x}} \quad (5)$$

where \mathbf{z} is the reduced-order state and \mathbf{U}_r is a matrix which contains the first r POD modes. When required, the full space density can be recomputed using Equation 6.

$$\mathbf{x}(\mathbf{s}, t) \approx \mathbf{U}_r(\mathbf{s}) \mathbf{z}(t) + \bar{\mathbf{x}}(\mathbf{s}) \quad (6)$$

The readers are referred to Mehta and Linares (2017) for additional information on the applications of the POD algorithm for thermospheric mass density prediction [10].

2.1.2 Machine Learning: Convolutional Autoencoder

An alternative method to POD which can be employed to obtain a reduced-order state is the use of an undercomplete autoencoder neural network. Undercomplete autoencoders have an encoded dimension that is less than the input dimension. An autoencoder encodes an input vector, X , as a reduced dimensional vector, V . Then, a reconstruction of the full-dimensional vector can be done via decoding V to X' [20]. Equation 7 defines the encoder portion of the autoencoder, \mathbb{F} :

$$\mathbb{F}: X \rightarrow V \quad (7)$$

To obtain the full-dimensional vector reconstruction, the decoder, \mathbb{G} , is employed:

$$\mathbb{G}: V \rightarrow X' \quad (8)$$

Both the encoder and decoder are found by minimizing the loss function \mathcal{L} :

$$\mathbb{F}, \mathbb{G} = \arg \min_{\mathbb{F}, \mathbb{G}} \mathcal{L}(X, X') \quad (9)$$

For this work, mean squared error is used as the loss function:

$$\mathcal{L}(X, X') = \frac{\|X - X'\|^2}{d} \quad (10)$$

where d is the dimension of the input vector and its reconstruction. The neural network is optimized using proximal policy optimization (PPO).

In contrast to POD, autoencoders are capable of learning nonlinear manifolds when given nonlinear activation functions. For a significant reduction in dimension, the advantages of capturing nonlinear features are more apparent. These advantages also come with the dangers associated with overfitting. A convolutional autoencoder architecture was utilized to leverage spatial information between the spatially correlated density data. Equation 11 describes the 2D convolution for the output, g , and the input, x .

$$g_{i,j,k,c} = \sigma(w_c^T x_{i,j,k,c}) \quad (11)$$

where $g_{i,j,k,c}$ is a data in the channel output and c is the filter.

Figs. 1a and 1b show the neural network architecture for the encoder network and the decoded network respectively. The encoder network consists of two 2D convolution layers and followed by three dense (fully connected) layers. The encoder network gradually condenses the data into a lower dimensional space via nonlinear embedding. Each layer uses the nonlinear Rectified Linear Unit (ReLU) activation function, except the final fully connected layer. A batch normalization layer is used after each 2D convolution layer. The batch normalization layer helps to make training more stable by re-centering and re-scaling the intermediate neural network outputs. On the other hand, the decoder network consists of two fully connected layers followed by three 2D transposed convolution layer. Each layers, except the final 2D transposed convolution layer, uses the nonlinear ReLU activation function. A batch normalization layer is used after the first two 2D transposed convolution layer.

2.1.3 Dynamic Mode Decomposition with Control

Dynamic Mode Decomposition with control (DMDc) is used in this work to propagate the reduced-order state forward in time by modeling the density data as a linear dynamical system. The future state is represented by Equation 12.

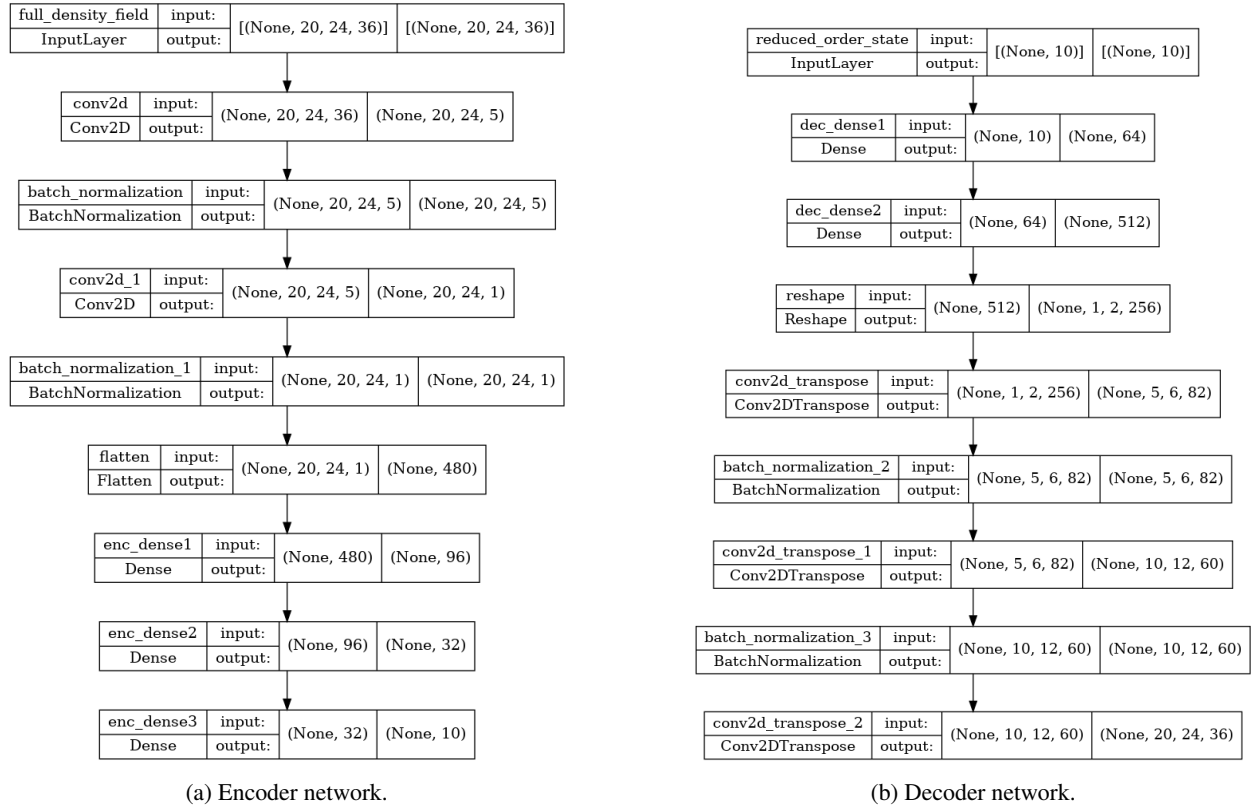


Fig. 1: Neural network architecture of the encoder and decoder network.

$$\mathbf{z}_{k+1} = \mathbf{f}(\mathbf{z}_k, \mathbf{u}_k) \quad (12)$$

where \mathbf{z}_k is the reduced-order state at epoch k (from Equation 5 or Equation 7). DMDc defines the dynamical system above in terms of a linear state and control input propagation:

$$\mathbf{z}_{k+1} = \mathbf{A}\mathbf{z}_k + \mathbf{B}\mathbf{u}_k \quad (13)$$

where \mathbf{u} , for this work, is the set of space weather indices and the dynamics matrix, \mathbf{A} , and the input matrix, \mathbf{B} , can be estimated from time-shifted state matrices:

$$\mathbf{Z}_1 = [\mathbf{z}_1 \ \mathbf{z}_2 \ \dots \ \mathbf{z}_{m-1}], \ \mathbf{Z}_2 = [\mathbf{z}_2 \ \mathbf{z}_3 \ \dots \ \mathbf{z}_m], \ \mathbf{Y} = [\mathbf{u}_1 \ \mathbf{u}_2 \ \dots \ \mathbf{u}_{m-1}] \quad (14)$$

where \mathbf{Z}_1 and \mathbf{Z}_2 are time-shifted snapshot matrices, m is the number of snapshots, and \mathbf{Y} is the set of inputs corresponding to \mathbf{Z}_1 . \mathbf{Z}_2 is defined by \mathbf{Z}_1 in the following way:

$$\mathbf{Z}_2 = \mathbf{A}\mathbf{Z}_1 + \mathbf{B}\mathbf{Y} \quad (15)$$

The matrices, \mathbf{A} and \mathbf{B} , can then be estimated using the method of least squares and the given values for \mathbf{Z}_1 and \mathbf{Z}_2 . The result is plugged into Equation 13 to obtain a linear reduced-order model for a fixed timestep, T .

A continuous dynamical model is required for density estimation:

$$\dot{\mathbf{z}} = \mathbf{A}_c\mathbf{z} + \mathbf{B}_c\mathbf{u} \quad (16)$$

where \mathbf{A}_c and \mathbf{B}_c are the corresponding continuous-time dynamic and input matrices. The continuous-time matrices are obtained using the relation from DeCarlo (1989) [21]:

$$\begin{bmatrix} \mathbf{A}_c & \mathbf{B}_c \\ \mathbf{0} & \mathbf{0} \end{bmatrix} = \log\left(\begin{bmatrix} \mathbf{A} & \mathbf{B} \\ \mathbf{0} & \mathbf{I} \end{bmatrix}\right)/T \quad (17)$$

where T designates the snapshot resolution or sample time.

Once the next state is predicted by DMDc (Equation 16), either Equations 5 and 6, for POD, or Equations 7 and 8, for the Autoencoder NN, can be used to map between the full and reduced-dimension spaces.

2.2 Density Estimation Toolbox: Reduced Order State Estimation

The Density Estimation Toolbox (DESTO) provides an open-source implementation of the POD-DMDc and ML-DMDc for estimation of global thermospheric density. The toolbox includes GPS, radar, or Two-Line-Element (TLE) data assimilation in the dynamic ROM model. The ROM state, orbit, and BC of a set of objects are simultaneously estimated using an Unscented Kalman Filter framework. The TLE data assimilation method for DESTO is shown in Figure 2. The ROM is generated using POD (see Section 2.1.1) or a convolutional autoencoder (see Section 2.1.2).

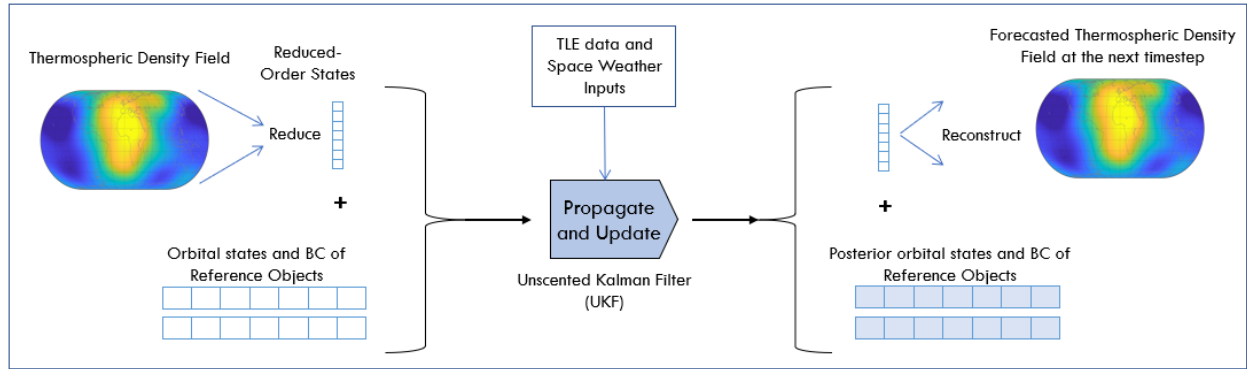


Fig. 2: DESTO global density estimation.

Then DMDc, from Section 2.1.3 is used to propagate the dynamic system forward, given the current atmospheric density state and space weather indices. The square-root unscented Kalman filter (UKF) is utilized to assimilate the density model and TLE data, for a specified set of space objects. Specifically, a UKF was chosen to reduce error in true posterior mean and covariance of the variables. The true posterior mean and covariance are computed to the third order by propagating a set of sigma points through the true nonlinear system dynamics. For an in-depth description of the UKF, see Wan and Van Der Merwe (2001) [22]. The UKF estimates the osculating orbital states, in modified equinoctial elements (MEE), the BCs of the list of objects, and the reduced-order density state, \mathbf{z} . See Gondelach and Linares (2020) for further information and DESTO performance specifications [11].

2.3 Ballistic Coefficient Estimation Theory

The technique used for BC estimation is a TLE-based method developed in [16]. In this method, a BC estimate is computed via a comparison between the change in semimajor axis observed between a pair of TLEs, and the predicted change in semimajor axis using a high-fidelity orbital propagator [16, 23]. At each step, the technique computes the change in semimajor axis between two TLEs, using the SGP4 propagator to convert TLEs into orbital elements. Next, the Accurate Integrator for Debris Analysis (AIDA) is used to propagate the satellite's state over the time period between the two TLEs. The perturbations used in the AIDA propagator include geopotential acceleration using the EGM2008 model, solar radiation pressure, sun and moon third-body perturbations, and atmospheric drag calculated with the NRLMSISE-00 density model. The propagation is accomplished using an initial guess for the BC. The AIDA-predicted change in semimajor axis is compared to the observed change in semimajor axis computed between the two TLEs, and the difference between the two is assumed to be due only to an incorrect guess for the BC. The estimated BC is updated using the Secant method, and the process is repeated iteratively until convergence.

In order to improve the quality of the BC estimates using this technique, Gondelach advocates for TLE preprocessing in the form of TLEs filtering to remove: 1) TLEs which were released and later corrected; 2) outliers in mean motion, perigee radius, and inclination; 3) large time gaps; 4) TLEs which are inconsistent with each other; and 5) TLEs with negative B-star values. Gondelach found that TLE pre-processing was important to the BC estimation process [16].

2.4 Orbit Propagation Theory

The propagator used for orbital reentry simulations was a modified version of the High Precision Orbital Propagator (HPOP) version 2.2.1, available on MATLAB Central File Exchange ³. This propagator uses the special perturbations approach to model the motion of an artificial satellite under the influence of orbital perturbations including non-spherical gravity, third-body effects, and atmospheric drag. Several modifications were made to the original HPOP to achieve consistency with the BC estimation process, including changing the integrator to ode113, switching the gravity model to EGM2008, and adding a deorbit condition to halt propagation at 100 km.

2.4.1 Force Model: Perturbations

The HPOP force model included the following perturbations. First, harmonic gravity terms up to degree 10 are computed with the EGM2008 model, neglecting the effects of solid Earth tides and ocean tides. Second, third-body perturbations from the sun and moon are computed using a point-mass model. Planetary third-body perturbations were not included. Solar radiation pressure was calculated using the assumption that the effective area for solar radiation pressure (SRP) given for a satellite is normal to the sun. Effective area for SRP is a user input. The shadow model for SRP is a geometric model computing the fraction of the solar disk as seen from the satellite, ranging between 0 (satellite fully in shadow) to 1 (satellite in full sun). Finally, drag is calculated using BC estimates computed with the technique discussed in the 2.3. For more implementation details of the BC estimation algorithm, see also 3.2. Drag is computed using a rotating atmosphere, with densities calculated by a range of atmospheric density models.

3. METHODS

Experimental methods for this study can be divided into three main categories: atmospheric density modeling, ballistic coefficient estimation, and satellite propagation.

3.1 Test Cases and Atmospheric Density Modeling

Deorbit test cases were chosen to reflect a variety of satellite configurations where reentry time was difficult to estimate. In addition, availability of documentation was of consideration when choosing each test case. The February Starlink deorbit event was chosen since it was in part due to changes in drag caused by a geomagnetic storm, ultimately resulting in an early reentry. Similarly, Humanity Star experienced high uncertainty in its reentry predictions. The high area-to-mass ratio and high reflectivity pose interesting parameters for reentry prediction. With a well-documented configuration and architecture, the Freedom dragsail Cubesat was chosen to analyze the effects of a dragsail on reentry.

Table 1 shows the list of atmospheric density models used for each test case.

Table 1: Atmospheric Density Models

Density Model	Type	Test Cases Applied
JB2008	Empirical	Starlink, Drag-Sail Cubesat, Humanity Star
NRLMSISE-00	Empirical	Starlink, Drag-Sail Cubesat, Humanity Star
POD JB2008 ROM	Reduced-Order	Starlink, Drag-Sail Cubesat, Humanity Star
ML JB2008 ROM	Reduced-Order	Starlink, Drag-Sail Cubesat, Humanity Star
POD TIE-GCM ROM	Reduced-Order	Starlink, Drag-Sail Cubesat, Humanity Star

3.1.1 Reduced-Order Model

The PODROM and MLROM reduce the dimensionality of the atmospheric mass density state space to a specified dimension. The initial atmospheric mass density state space consists of an array of density data evaluated at different latitudes, local solar times, and altitudes. The POD models are trained for the JB2008 and TIE-GCM density models using the methods outlined in Gondelach and Linares [11]. MLROMs are constructed by first designing a Convolutional Neural Network (CNN) architecture for the Autoencoder and then training the ROM on the atmospheric mass

³ Available at <https://www.mathworks.com/matlabcentral/fileexchange/55167-high-precision-orbit-propagator>

density state data until acceptable training and test set errors are achieved. The CNN architecture employed for this analysis is described in 2.1.2. MLROMs take significantly longer timeframes for training when compared to PODROMs. Therefore, only a single MLROM based on the empirical JB2008 model was studied in this work. The spatial resolution of the different atmospheric density training data used are shown in Table 2. Training data for both ROM types uses an hourly temporal resolution. Reduced order density states for PODROMs are in double precision, while MLROM reduced order states are in single precision due to limitations of MATLAB's Deep Learning Toolbox.

Table 2: Spatial Resolution of the Different Atmospheric Density Training Data

Model	Local solar time (hr)		Latitude (deg)		Altitude (km)		Period
	Domain	Resolution	Domain	Resolution	Domain	Resolution	
JB2008	[0, 24]	1.04	[-87.5, 87.5]	9.20	[100, 800]	20	1999 - 2010
TIE-GCM	[0, 24]	1	[-87.5, 87.5]	9.2	[100, 450]	17.5	1997 - 2008

3.1.2 Space Weather Inputs

Space weather activity is the main driver for atmospheric density propagation. Table 3 shows the list of space weather indices used by the various atmospheric density models studied in this work as their primary inputs. The space weather indices function as proxy to represent the level of space weather activities.

Table 3: Space Weather Inputs

Index	Description	Models Used
$F_{10.7}$	Solar radio noise flux at a wavelength of 10.7 cm	JB2008, POD TIE-GCM ROM, NRLMSISE-00
S_{10}	Activity indicator of the integrated 26–34 nm solar irradiance	JB2008
M_{10}	Modified daily Mg II core-to-wing ratio	JB2008
DSTDTC	Temperature change calculated from the Disturbance Storm Time (DST) Index	JB2008
kp	3-hour-range standardized quasi-logarithmic magnetic activity	POD TIE-GCM ROM
ap	3-hourly magnetic activity index derived from kp	NRLMSISE-00

For ROM propagation with DMDc, additional future (next-hour) and nonlinear space weather indices were used and are shown in Table 4. As demonstrated in [11], the usage of future and nonlinear space weather indices improve the accuracy of the DMDc prediction. These nonlinear space weather indices were used as inputs for all ROM models.

Table 4: Additional Space Weather Inputs Used for the DMDc Models

ROM Model	Standard input	Future input	Nonlinear input
JB2008	doy, hr, $F_{10.7}$, $\bar{F}_{10.7}$, S_{10} , \bar{S}_{10} , M_{10} , \bar{M}_{10} , Y_{10} , \bar{Y}_{10} , $DSTDTC$, $GMST$, α_{sun} , δ_{sun}	$F_{10.7}$, S_{10} , M_{10} , Y_{10} , $DSTDTC$	$DSTDTC^2$, $F_{10.7} \cdot DSTDTC$
TIE-GCM	doy, hr, $F_{10.7}$, $\bar{F}_{10.7}$, kp	$F_{10.7}$, kp	kp^2 , $kp \cdot F_{10.7}$

Note. doy = day of year; hr = hour in UTC; GMST = Greenwich Mean Sidereal Time. Overbars indicate the 81-day average. Nonlinear inputs are constructed using both current inputs and future inputs.

To test each model's sensitivity to noise in space weather inputs, a Gaussian noise model was constructed and added to the true space weather indices. The predicted deorbit times and propagated orbits were compared for each test case to verify each atmospheric density model's performance under input uncertainties.

3.1.3 Density Estimation Toolbox for Reduced-Order State Estimation

TLE orbital data assimilation with the dynamic ROM model was performed by the DESTO Toolbox. The objects used for density estimation are included in Table 5.

Table 5: Objects used for density estimation

NORAD catalog ID	Object	BC m^2/kg	Perigee km	Apogee km	Inclination deg
22	Explorer 7	0.02297	486	680	50.3
614	Hitchhiker 1	0.01463	300–299	1,096–1,092	82
932	Explorer 25	0.02118	523–522	2,285	81.3
1807	Thor-Agena B R/B	0.0255	500	2,648–2,647	79.8
2153	Thor-Agena B DEB	0.03329	499–498	2,563–2,562	79.7
2389	OV3-3	0.0181	337	2,230–2,229	81.4
4221	Azur	0.02201	353	1,242–1,241	102.7
4382	DFH-1	0.01105	428	2,032–2,031	68.4
7337	Vektor	0.0112	373–372	1,147–1,146	82.9
8744	Vektor	0.01117	368–367	1,187–1,186	82.9
12138	Vektor	0.01115	388–387	1,425–1,424	83
12388	Vektor	0.01121	384–383	1,425–1,424	82.9
14483	Vektor	0.0113	383–382	1,476	82.9
20774	Vektor	0.01168	391–387	1764–1684	83
23278	Vektor	0.01168	393–392	1,698	83
41771	SkySat C4	0.01626	452	454	97.21
41772	SkySat C5	0.01626	490	493	97.4
41773	SkySat C2	0.01626	451	454	97.21
42988	SkySat C10	0.01626	448	455	97.24
42989	SkySat C9	0.01626	451	452	97.23
42992	SkySat C6	0.01626	451	452	97.24
43797	SkySat C12	0.01626	452	454	97.21
39418	SKYSAT 1	0.01626	559.7	589.9	97.6
40072	SKYSAT 2 or B	0.01626	627.2	634.8	98.4148
41601	SKYSAT-C1	0.01626	457.4	462.1	97.156

The objects are chosen based on availability of accurate BCs for each object, small variations in BC over time, and strong drag signals. All objects, except the addition of five SkySats, are from Gondelach and Linares (2020) [11]. Figure 3 shows a visualization of the object list. A wide range of orbit types were chosen to allow for an accurate global atmospheric density estimate. Both the entire set of 25 objects as well as the original 5 from Gondelach and Linares (2020) were analyzed for reduced-order state estimation and used for reentry prediction [11].

3.2 Ballistic Coefficient Estimation

Prior to BC estimation, TLEs for all three satellite cases were preprocessed using all of the filter types mentioned in 2.3: corrected TLEs, large time gaps, outliers, inconsistent TLEs, and TLEs with a negative B-star [16]. This filtering resulted in a significant number of TLEs being removed during the BC estimation process. For example, in the case of the Starlink satellite, only 15 out of the original 25 available TLEs were used for BC estimation. BC estimation for each of the three satellite test cases was then conducted using the technique described in 2.3 and further detailed in [16, 23]. The BC estimates computed from TLEs falling within each simulation time frame (the 5-day period leading up to the last available TLE before reentry, for each respective satellite) were used to compute a BC model for the duration of the simulation. The BC estimates for Starlink 51470 and Humanity Star were relatively stable during the simulation time frame, exhibiting changes of not more than $0.015 m^2/kg$ and $0.15 m^2/kg$, respectively. A plot of BC throughout simulation duration is shown for all three satellite test cases in Fig. 4. Due to their relatively stable BCs during the simulation window, a simple arithmetic mean of the BCs computed within the simulation time frame was selected as the BC model for the Starlink and Humanity Star satellites.

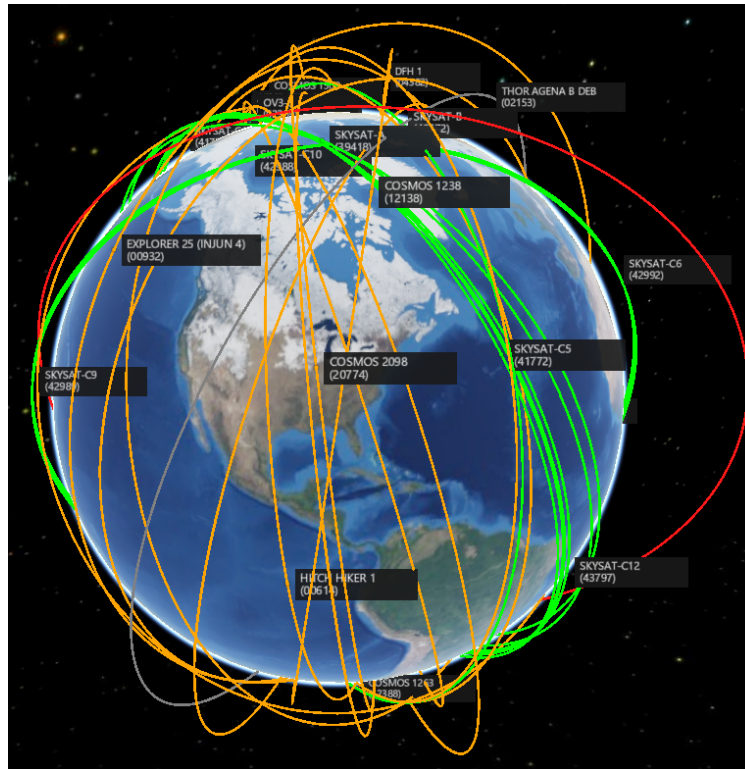


Fig. 3: Orbit visualization of the DESTO object list [24].

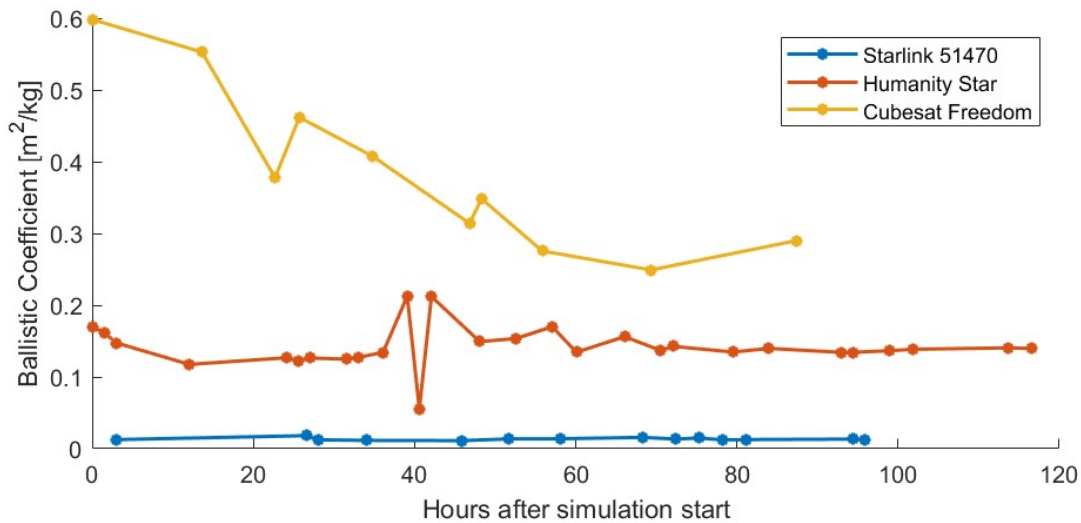


Fig. 4: Ballistic coefficient (BC) throughout simulation duration for Starlink 51470, Humanity Star, and Cubesat Freedom.

However, in the case of the Cubesat Freedom, the mean BC was a poor descriptor of the BC behavior over time. The Cubesat's BC was more difficult to accurately model since it was much higher than the other BCs and changed rapidly near the end of its orbit. During the simulation time frame, its BC dropped by almost $0.4 m^2/kg$ prior to stabilizing at a lower value. An orbital analysis by the satellite operators on the results of the Cubesat mission suggested that the satellite may have experienced an unplanned configuration change during its deorbit, causing the sudden drop in the

BC [25]. Due to the changes in BC over time, a linear model for BC was used for the Cubesat instead of the mean BC. This linear model was fit using all available BC estimates, including those calculated from TLEs prior to the start time of the deorbit simulation. The reason for including all available BC estimates was to prevent the linear model from dropping off rapidly to nonphysical negative values due to the sudden decrease in BC just before deorbit.

3.3 Satellite Propagation

For each of the three satellite test cases, an initial state was derived from a TLE occurring approximately 5 days before the last-available TLE for the respective object. The SGP4 propagator was used to convert from the TLE state to the ECI initial state for propagation. Satellite propagation from this initial state was conducted for each model and satellite until atmospheric re-entry, defined in this study as the point at which the satellite's altitude drops below 100 km.

3.3.1 Consistency between propagation and BC estimation

To maintain consistency between the BC estimate and the satellite propagation, we modified the HPOP propagator to match its specifications to those of the AIDA propagator used for BC estimation. The table below summarizes the two propagators.

Table 6: HPOP vs AIDA Propagators

Parameter	HPOP (Propagation)	AIDA (BC Estimation)
Integrator	ode113	ode113
Gravitational Harmonics Model	EGM2008	EGM2008
Gravitational Harmonics Degree	10	10
Third Body Effects	Sun, Moon	Sun, Moon
SRP Used	Yes	Yes
SRP Earth Shadow Model	Geometric	Biconical
Atmospheric Drag Model	Rotating Atmosphere	Rotating Atmosphere
Atmospheric Density Model	Various	NRLMSISE-00

The satellite parameters used in each of the three cases, such as mass, SRP effective area, and C_r , were the same for propagation and BC estimation and are provided in Table 7. The estimated ballistic coefficient values (generated by BC estimation and used in propagation) are also shown in Table 7. A default C_r value of 1.0 was assigned to the Starlink and Cubesat satellites. A higher C_r value of 1.04 for the Humanity Star was selected based on an analysis of the Ajsai satellite, which had a similar high-reflectivity mirrored surface [26]. The mass and dimensions of the Starlink Satellite were not publicly released, so we used estimates based on a Starlink stack image⁴. Humanity Star mass and frontal area estimates were derived from size and weight estimations found in an article on the satellite's premature deorbit⁵. Cubesat mass and frontal area estimates are taken from an analysis of its deorbit and drag sail efficacy [25]. The BC estimates used for propagation in the Starlink and Humanity Star cases were constant values, while in the Cubesat case a linear model was used, as discussed in Section 3.2. This linear model is given in the table below, where x is the number of hours since the start time of the simulation.

Table 7: Satellite parameters used in propagation

Parameter	Starlink	Humanity Star	Cubesat Freedom
Satellite SRP Coefficient (C_r)	1.0	1.04	1.0
SRP Effective Area	0.3200 [m^2]	0.7854 [m^2]	0.6400 [m^2]
Satellite Mass	260 [kg]	10.5 [kg]	1.3 [kg]
Ballistic Coefficient Model	0.0135 [m^2/kg]	0.1421 [m^2/kg]	$-0.0013x + 0.5545$ [m^2/kg]

⁴Values taken from <https://lilibots.blogspot.com/2020/04/starlink-satellite-dimension-estimates.html> [Accessed on 19 July 2022]

⁵Values taken from <https://www.theatlantic.com/science/archive/2018/03/humanity-star-satellite-crash/555965/> [Accessed 28 June 2022]

3.3.2 Density Models in Satellite Propagation

Two distinct processes exist for retrieving an atmospheric density value in the drag calculation used by this modified version of HPOP. The first process involves running an atmospheric model directly for a given time, position, and set of space weather conditions. This process was used in the case of the JB2008 and NRLMSISE-00 density models.

The second process, used for every type of ROM, was a two-step process, involving a) updating the ROM state using DMDc and space weather inputs along with MATLAB's ode113 integrator, and b) using the ROM state to calculate a density value for the requisite time and position. In the case of the PODROMs, linear interpolation in the reduced-order space was used to find the ROM state at each desired time. In the case of the JB2008-based MLROM, interpolation was conducted in the full density space due to the nonlinear nature of the autoencoder. Reduced-order states were updated every 1 minute for the PODROMs, and every 15 minutes for the MLROM, due to the longer run time of the MLROM.

3.4 Adding Noise to Space Weather Inputs

To evaluate the sensitivity of the atmospheric models to noise in space weather inputs, we conducted an analysis using three density models: the JB2008, the JB2008-based PODROM, and the JB2008-based MLROM. For these models, the space weather indices F10, S10, M10, and Y10 were perturbed using a zero-centered Gaussian noise model, with a new set of noise values calculated at hourly intervals. The 81-day averaged values for these indices are also model inputs for the JB2008 and JB2008-based models, but these values were not perturbed since the noise model was centered at zero. Reference space weather data taken from the CIRA-08 was used to estimate the standard deviation in noise for the indices mentioned above [27], with the assumption that the difference between the tabulated maximum and minimum values of each index represents a 6-sigma spread in index values. The tabulated values used were determined by the relative month number in the solar cycle, with December 2008 and December 2019 used as the start dates of Solar Cycles 24 and 25, respectively [28, 29].

In the case of the JB2008-based PODROM and MLROM, the reduced-order state is initialized using a global density “snapshot” generated using the JB2008 model. For the sensitivity analysis, this snapshot was also generated with perturbed space weather inputs. The JB2008 model does not require initialization.

To produce approximately equivalent noise values across the ROM and JB2008 cases, a shared seed was specified for the random noise generation. Space weather input noise cannot be applied in the same way across all density model cases, since the JB2008 model takes inputs with a time lag, while the ROMs take real-time data. Therefore, noise values were assigned to 1-hour time windows, and added directly to the space weather inputs of each model, irrespective of time lags in the inputs. In theory, this creates perturbations of equal magnitude during equal time frames, across all models. In practice, the variable internal time step of the propagator may cause discrepancies in the times at which new noise values are generated, but these discrepancies are small (on the order of a few seconds).

Simulations were also performed with tabulated reference space weather values from CIRA-08. The reference values used were mean observed monthly values from Solar Cycle 23, considered a moderately active cycle [27].

4. RESULTS

A limiting factor in evaluating results for this study was the lack of availability of high-quality data, such as GPS or radar tracking measurements. The only available data in each case was TLE data, which suffers both from its relatively low quality and from its sparsity. Measures of success by quantitative comparison to TLE data therefore suffer both from 1) potential TLE error, and 2) the lack of TLEs at or near reentry altitude (100 km). The latter problem is addressed here by fitting a double exponential curve of the form $a \exp(bx) + c \exp(dx)$ to the final 50 hours of TLE data for each satellite test case in order to approximate a reentry time via extrapolation from the TLEs. While this measure does not provide a true reentry time, it is an improvement over comparing final-TLE time (at an altitude of 150+ km) to predicted reentry times (at 100 km). Since none of the three satellite test cases had an associated reentry campaign, extrapolation from TLE data represents the “best effort” reentry time prediction, given data limitations. We will compare density model performance on the basis of consistency with the TLE-extrapolated reentry time, with the caveat that a “best” model cannot be selected from a set of similar performers, given the uncertainty in the true reentry time.

4.1 Humanity Star

The results for all models used in the Humanity Star case are shown in Fig. 5.

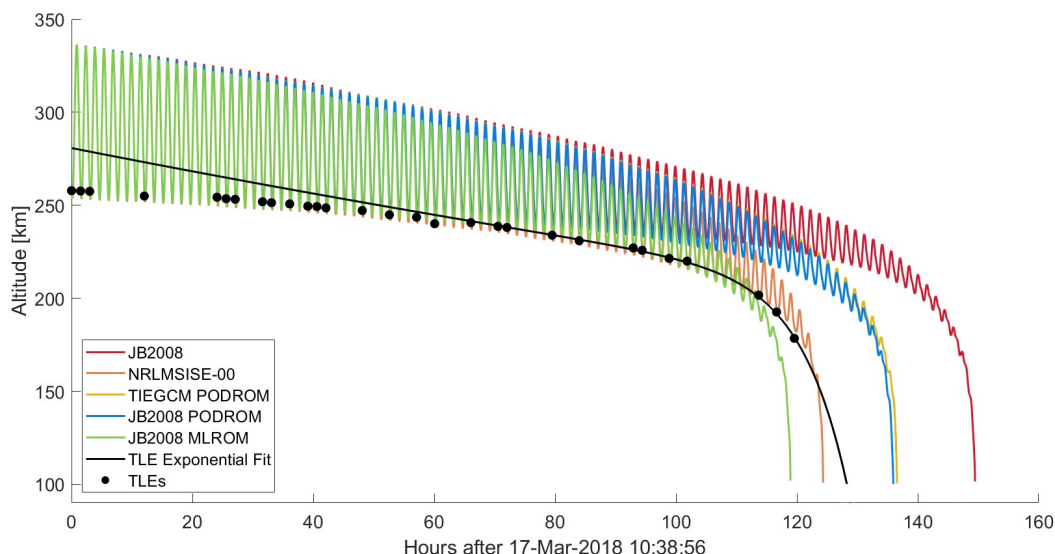


Fig. 5: Comparison of Humanity Star trajectory using varying atmospheric density models.

The reentry time predictions of the three ROM models all fell within a window of ± 10 hours of the TLE-extrapolated reentry time at 18:44 UTC on 22 March 2018. The MLROM predicted reentry before, and the PODROMs predicted after, the TLE-extrapolated reentry time. In the Humanity Star case, however, the prediction window was approximately four times larger than in the Starlink case. The NRLMSISE-00 predicted reentry at about 15:00 UTC on 22 March, making its prediction the closest to the TLE-extrapolated reentry time. The JB2008 model overshoot the TLE-based reentry by 21.2 hours. The ROM models averaged an 8.5-hour difference from the TLE-based reentry time, while the two non-ROM models produced both the closest and furthest predictions, averaging to a 12.6-hour difference.

The results of using noisy and reference space weather values are shown in Fig. 6. The MLROM shows the least overall impact from noisy or reference space weather, with approximately a 30-hour spread between its earliest and latest predictions, as compared to a 44-hour spread for the PODROM and a 45-hour spread for the JB2008. The JB2008 is again the least sensitive to noisy space weather.

4.2 Cubesat Freedom

For the time frame of the Cubesat Freedom test case, simulations were run using the same set of models used for the Humanity Star test case. The results are shown in Fig. 7. In the Cubesat Freedom case, the final 52 hours of TLE data were used for the double exponential fit, instead of the final 50 hours, in order to include at least 5 data points in the fit.

Once again, the JB2008 and TIE-GCM PODROMs show very similar performance. In addition, both PODROMs and the MLROM predict reentry within a 1.5-hour window; however, unlike in the other test case, this window is not close to being centered on the TLE-extrapolated reentry time at 07:44 UTC on 6 February 2017. Instead, the three ROM reentry predictions center on 13:37 UTC on 5 February, with an average undershoot of about 18 hours as compared to the TLE-extrapolated reentry time. This test case is also the only one in which these two PODROMs undershoot the reentry. Another distinguishing feature of the Cubesat Freedom test case is the large 35-hour gap in reentry time predictions between the JB2008 and the two PODROMs. Notably, all of the models have difficulty keeping consistency with the TLEs in the Cubesat Freedom test case: only the NRLMSISE-00 predicts reentry within ± 10 hours of the TLE-extrapolated time. Both of the non-ROM models overshoot the TLE-extrapolated reentry time, with an average overshoot of about 11 hours.

The results of using noisy and reference space weather data in the Cubesat Freedom case, shown in Fig. 8, closely mimic results from the previous test case: the MLROM again showed the lowest overall impact, with about a 14.5-hour

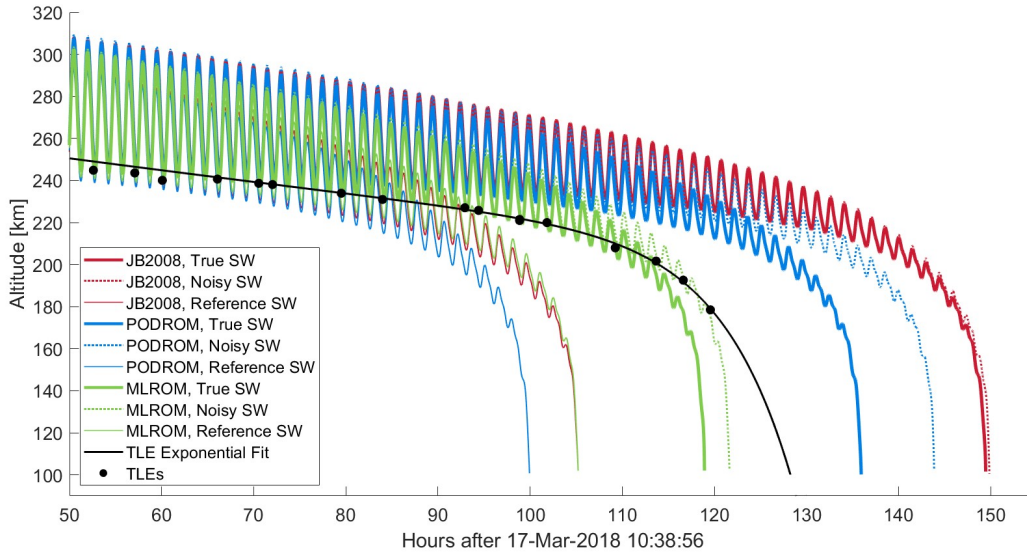


Fig. 6: Close-up comparison of Humanity Star trajectory using JB2008 and JB2008-based atmospheric density models with true space weather values, with random Gaussian zero-centered noise added to space weather indices, and with reference space weather values (F10, S10, M10, and Y10).

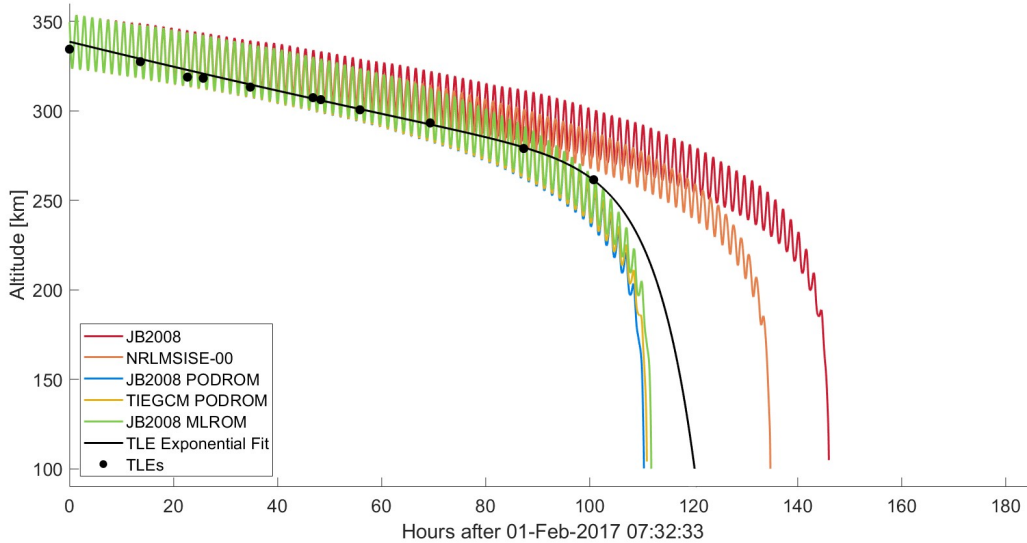


Fig. 7: Comparison of Cubesat Freedom trajectory using varying atmospheric density models and a linear ballistic coefficient model.

spread between its earliest and latest reentry time predictions, as compared to a 37.4-hour spread for the PODROM and a 40.8-hour spread for the JB2008. The JB2008 again had the least sensitivity to noisy space weather data, but a much greater change due to the use of reference space weather data. As in the previous case, the use of reference values resulted in an earlier reentry time prediction for all models, while the use of noisy values led to a later reentry time prediction.

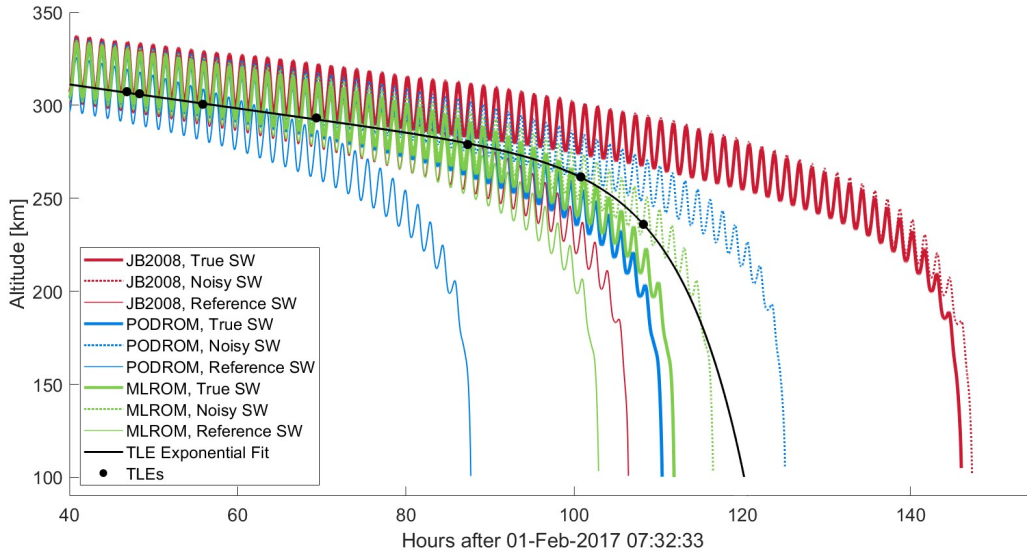


Fig. 8: Close-up comparison of Cubesat Freedom trajectory using JB2008 and JB2008-based atmospheric density models with true space weather values, with random Gaussian zero-centered noise added to space weather indices, and with reference space weather values (F10, S10, M10, and Y10).

4.3 Starlink 51470

The Starlink test case, shown in Fig. 9, examined the three non-ROM density models as compared to three ROM models.

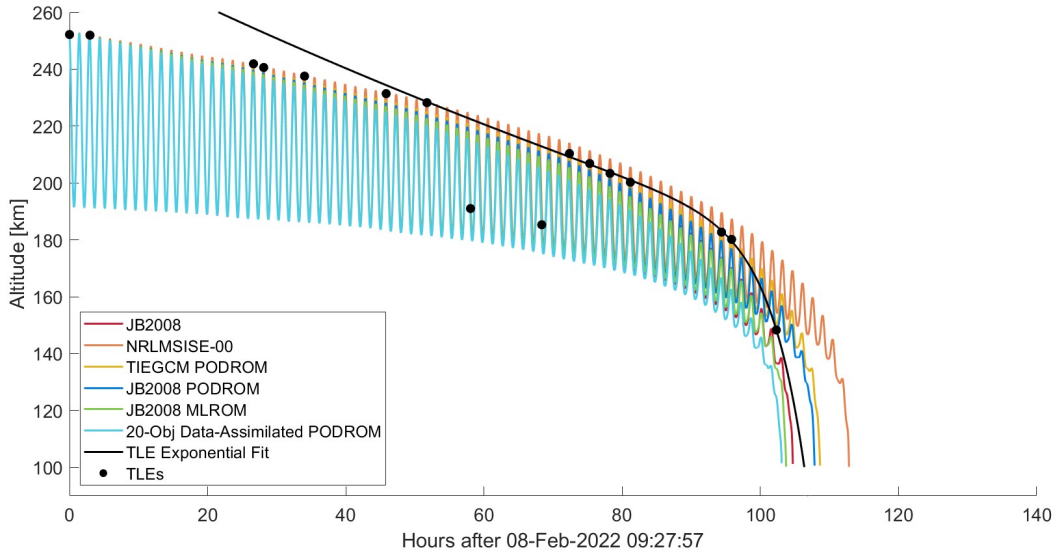


Fig. 9: Comparison of Starlink 51470 trajectory using varying atmospheric density models.

The JB2008 and the ROMs demonstrate relatively similar performance, with JB2008 and the ROMs all predicting reentry within about a 5-hour window centered on 12 February 2022 at approximately 19:20 UTC. The TLE-extrapolated reentry time occurred at about 19:40 UTC, placing it within minutes of the center of this 5-hour prediction window. These results are similar to the previous cases, the NRLMSISE-00 showed a 6.5-hour delay with respect to the ROMs,

predicting reentry at approximately 02:17 UTC on 13 February. For a comparison, the reentry predictions fell within a 35-hour window in the Cubesat Freedom case, and a 14.5-hour window in the Humanity Star case. On average, ROM models and non-ROM predicted reentry within ± 2.2 hours and ± 11.5 hours of the TLE-extrapolated reentry time, respectively.

Further simulations included comparisons between differing ROM types, including a data-assimilated ROM which was calibrated using 20 reference objects. The ROM state used for calculations was updated by importing the ROM state for the relevant time from a table of pre-propagated states. The data-assimilated ROM was consistent with the TLE-extrapolated reentry time for the Starlink case, with a difference in reentry prediction of 3.2 hours. Future work applying this model to additional test cases would allow more thorough analysis of the use of data assimilation in calibrating ROMs.

Fig. 10 shows the variation in predicted reentry time due to inaccurate space weather indices. Of the three models tested with noisy and tabulated reference space weather values (for F10, S10, M10, and Y10), the MLROM demonstrated the lowest impact overall from the use of noisy or reference values, as measured by the spread between earliest and latest prediction. Its predicted reentry time in both cases changed by less than 3 hours, although in different directions. Reference space weather values led to an earlier reentry time, while noisy space weather led to a later reentry time. The JB2008 model showed the lowest sensitivity to noisy space weather, with the prediction time changing by only half an hour in the presence of noise. However, the use of reference space weather values caused a change of almost 13 hours. The JB2008-based PODROM showed the greatest change in both the noisy and reference space weather cases, deviating from its original prediction by 6.7 and 14.7 hours, respectively.

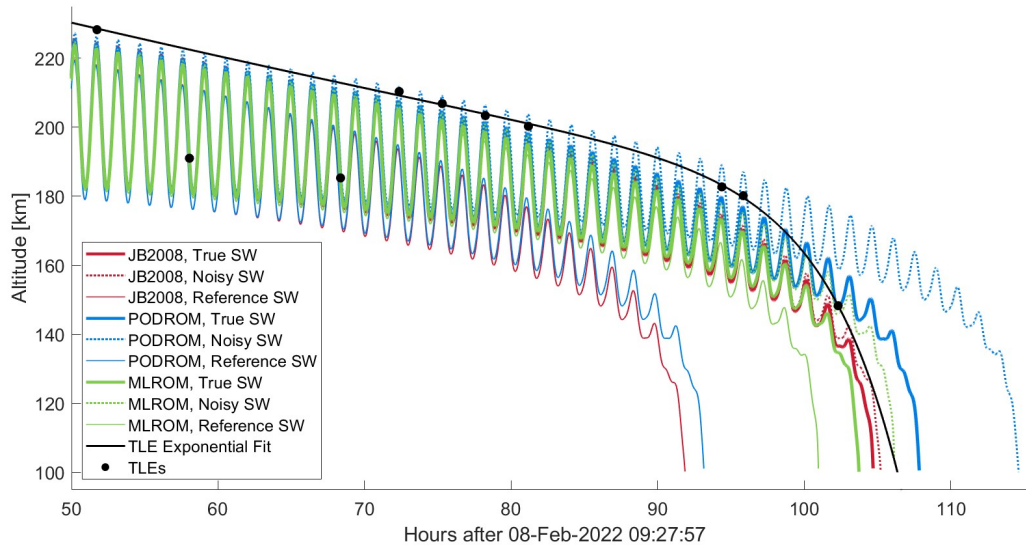


Fig. 10: Close-up comparison of Starlink 51470 trajectory using JB2008 and JB2008-based atmospheric density models with true space weather values, with random Gaussian zero-centered noise added to space weather indices, and with reference space weather values (F10, S10, M10, and Y10).

5. DISCUSSION

5.1 Comparison of Density Models

The snapshot of reentry time prediction by all models, for all test cases, is shown in Table 8. Of all models used, the NRLMSISE-00 was the second most consistent performer across all three test cases, with an RMS difference of 9.5 hours from the TLE-extrapolated reentry time. This model's relatively good performance is an expected result, since the NRLMSISE-00 has an "unfair advantage" over other models due to its use in the BC estimation process. Because of the assumption that erroneous BC is the only source of disagreement between TLE-derived and AIDA-predicted semi-major axis change, BCs estimated with this process absorb error from the density model used in the

Table 8: Snapshot of reentry time predictions for all test cases

Hours after Simulation Start							
	Starlink 51470		Humanity Star		Cubesat Freedom		RMS ΔTLE Fit
TLE Reentry Time (Exponential Fit)	106.3		128.3		120.2		
	Predicted Reentry	ΔTLE Fit	Predicted Reentry	ΔTLE Fit	Predicted Reentry	ΔTLE Fit	
JB2008	104.7	-1.6	149.5	21.2	146.0	25.8	19.3
with Noisy SW	105.2	-1.1	149.9	21.6	147.3	27.1	20.0
with Reference SW	91.9	-14.4	105.2	-23.1	106.5	-13.7	17.6
NRLMSISE-00	112.8	6.5	124.4	-3.9	134.8	14.6	9.5
JB2008 PODROM	107.9	1.6	136.0	7.7	110.5	-9.7	7.2
with Noisy SW	114.6	8.3	143.9	15.6	125.1	4.9	10.6
with Reference SW	93.2	-13.1	99.9	-28.4	87.7	-32.5	26.0
TIE-GCM PODROM	108.7	2.4	136.6	8.3	111.0	-9.2	7.3
20-Obj Data Assimilated PODROM	103.1	-3.2	N/A	N/A	N/A	N/A	N/A
JB2008 MLROM	103.7	-2.6	118.9	-9.4	111.9	-8.3	7.4
with Noisy SW	106.2	-0.1	121.7	-6.6	116.5	-3.7	4.4
with Reference SW	101.0	-5.3	105.2	-23.1	102.9	-17.3	16.9

AIDA propagation. Since NRLMSISE-00 is used by AIDA, the BCs estimated using AIDA partially compensate for error in this model, making these BC estimates compatible with the NRLMSISE-00 model. Gondelach notes that BCs estimated using this technique should be paired with the model used in estimation [16]. The relative success of the NRLMSISE-00 model in the three test cases may be aided by this effect. BC estimates using the other models were not available for this project, but are an important direction for future work in order to develop more equivalent comparisons of density models.

The three ROM models were the highest performers by a small margin in terms of consistency with the TLE-extrapolated reentry time. All three had an RMS difference of between 7 and 8 hours from the TLE-based reentry time. Furthermore, the TIE-GCM PODROM and JB2008 PODROM show most similar results, with reentry times agreeing to within one hour for all test cases. One hypothesis for the cause of this similarity is that these two ROMs use the same data to initialize the reduced-order density state. Since the JB2008-based and TIE-GCM-based PODROMs were generated from different models, their reduced-order state updates differ; however, they both use a density field snapshot from the JB2008 model to initialize the reduced-order state at the simulation start time. The use of JB2008 to generate initialization data in both PODROM cases is due to its much lower computational cost, as compared to the physics-based TIE-GCM. This hypothesis suggests that for short-term propagation, the initial ROM state dominates calculated densities compared to the effect of ROM state updates, and thus ROMs initialized on the same data are likely to yield similar reentry prediction results. While the MLROM is also initialized on the same data, its different method of encoding reduced-order states may account for its relative dissimilarity from the two PODROMs. Closer examination of the PODROM similarity represents another area for further research.

A notable trend in the overall model performance is the decreasing agreement of reentry predictions with the TLE-extrapolated reentry time as ballistic coefficient increases. For the Starlink case, with the lowest BC, the RMS difference across all density models between TLE-based reentry time and predicted reentry time was 3.4 hours, with a median difference of ± 2.5 hours. This increased for the Humanity Star to an RMS 11.7-hour difference and a median ± 8.3 -hour difference. Finally, for the Cubesat Freedom, which had the highest BC by far due to its drag sail and small mass, the RMS difference was 15.0 hours and the median was ± 9.7 hours. The greater difficulty in reentry simulations of high-BC objects is expected, as a large BC magnifies the relative importance of the drag force in determining the object's orbit. As a result, a larger BC increases the impact of small changes in density values, resulting in a greater impact from density model error.

While the overall performance and the performance of all ROMs trended downward with increasing BC, the NRLMSISE-00 model did not match this pattern exactly. It demonstrated its lowest difference from the TLE-extrapolated reentry time in the case of the Humanity Star (-3.9 hours) as compared to the other two cases (6.5 and 14.6 hours, respectively). Again, while the agreement of the NRLMSISE-00 model with TLE-extrapolated reentry times varied across the three cases, its generally good performance as measured by RMS difference may be due to its use in modeling BC.

A final point of interest is that in all cases, reference space weather values resulted in a greater undershoot relative to true-SW predictions and noisy values resulted in either a relative overshoot or a much smaller undershoot. This indicates that the reference space weather led to slightly higher density values, while noisy SW caused lower densities. Note that for the noisy case, this is not necessarily a general trend. The set of noise values used in this simulation is only a single set of randomized noise; a different set of noise values would cause different simulation results. Ideally, Monte Carlo simulations would be conducted using many sets of randomized noise to examine the general effects of space weather noise on reentry predictions. However, this analysis was not conducted as part of this work due to time constraints. While these results are not representative of the effect of space weather noise in general, we can observe the relative sensitivity of the models to noise.

5.2 Impact of Noisy and Tabulated Reference Space Weather Inputs

In general, all models tested with noisy and reference space weather demonstrated greater impact from the reference values than from the noisy values. This is likely because in most cases, the reference space weather values significantly overestimate the true values. This effect is particularly notable in the Humanity Star and Cubesat Freedom cases, which occurred near the end of Solar Cycle 24, the 4th-weakest solar cycle on record [28, 29]. The tabulated reference data represents mean monthly observed values from Solar Cycle 23, considered a moderate cycle [27]. Using these values during Solar Cycle 24, a remarkably weak cycle, leads to chronic overestimation of the SW values. The higher density estimations resulting from the high SW index values caused higher drag forces and earlier reentry. For plots of true, noisy, and reference space weather indices, see Figs. 11, 12, and 13 in Appendix A.

One hypothesized reason for the relative sensitivity of the ROMs to noise in the space weather inputs is the implementation of noise in the JB2008 snapshot used to initialize the ROM state. This means that the initial ROM state contains a bias associated with the particular noise values used to initialize it. No matter how accurate the ROM state updates are, it may prove difficult for these updates to overcome the initial bias caused by the noise present during initialization, especially in short-duration simulations. One direction for future research is to evaluate the relative sensitivity of ROM reentry predictions to initial-state space weather noise as compared to noise in space weather inputs used to update the ROM state following its initialization. This analysis may also shed light on the impact of initialization data in general on the performance of ROMs, as discussed in Section 5.1. It may be possible to improve ROM performance in an operational context by initializing the ROM state using true space weather values at a past time, then propagating the ROM state into the future using predicted space weather values (which may be regarded as “noisy” due to prediction error), instead of initializing and propagating the ROM based on predicted values.

6. CONCLUSION

This work has demonstrated the use of atmospheric density modeling for accurate drag prediction, ultimately resulting in a software architecture which enables space weather-informed reentry predictions for RSOs. Empirical and physics-based density models were compared with ROMs for three reentry prediction test cases (Starlink 51470, Humanity Star, and Cubesat Freedom). Generally, the Starlink deorbit test case yielded the closest predicted reentry times to the TLE-extrapolated time, with differences primarily between 1-7 hours. Cubesat Freedom had the largest difference in predicted and TLE-based reentry times across most models, with differences ranging from 8.3 hours to 25.8 hours. The use of noisy and reference space weather indices generally degraded the prediction accuracy of most models. Even with the presence of noise, JB2008 and the JB2008 PODROM were able to obtain reentry predictions close to the RMS prediction obtained using the true space weather indices. In addition, the JB2008 MLROM showed the lowest overall spread from the earliest to latest reentry predictions. From these preliminary results, reentry prediction in real-time, without access to true space weather indices, is feasible.

Based on the criteria of RMS difference between model-predicted reentry time and TLE-extrapolated reentry time, the NRLMSISE-00 density model was the top performer when paired with a BC derived using the NRLMSISE-00 model. With the same BC, the three ROMs showed similar RMS results and out-performed the JB2008 model. These results are not sufficient to draw conclusions regarding the performance of the NRLMSISE-00 model absent the confounding

factor of its use in BC estimation. In addition, the similar results of the two PODROMs in all cases suggest that some shared factor may influence both models. Since the reference space weather values tend to degrade reentry time predictions when they are consistently far from the true values, reference values should be sourced from a solar cycle with a similar activity level to the cycle of interest.

Based on our results, several directions exist for further research. First, improvements on the current study by identifying satellite test cases with higher-quality data, such as GPS or radar tracking measurements, would overcome the accuracy limitations of TLE data. Secondly, BC estimates can be improved by using all density models to estimate a BC and taking the average of the estimated BCs. This would remove the problem of BCs absorbing error from the NRLMSISE-00 model and allows for the assessment of the BC estimation algorithm for compensation of density modeling errors. Another direction for future investigation is the inclusion of additional models, such as TIE-GCM, HASDM, WAM-IPE, and additional ROMs with data assimilation. An additional space weather input sensitivity analysis, with a Monte Carlo simulation, would also be valuable to verify the preliminary results in this work. Finally, the similarity between PODROMs and the hypothesis regarding relative importance of initialization data could be explored by attempting to isolate the effects of reduced-order state initialization from the effects of reduced-order state propagation. Possible methods for such an investigation include 1) evaluating the impact of initializing ROMs with NRLMSISE-00 data instead of JB2008 data, and 2) using true space weather data in reduced-order state initialization, but noisy space weather inputs for propagation.

ACKNOWLEDGEMENT

This work was supported by a NASA Space Technology Graduate Research Opportunity and the National Science Foundation under award NSF-PHY-2028125. Author Nicolette Clark's graduate education is supported by the MIT Lincoln Laboratory Military Fellows Program. The authors would like to thank the MIT SuperCloud and Lincoln Laboratory Supercomputing Center for providing HPC, database, and consultation resources that have contributed to the research results reported in this paper.

REFERENCES

- [1] Aaron Boley and Michael Byers. Satellite mega-constellations create risks in low earth orbit, the atmosphere and on earth. *Scientific Reports*, 11:10642, 05 2021.
- [2] J.T. Emmert. Thermospheric mass density: A review. *Advances in Space Research*, 56, 06 2015.
- [3] Balch C., Biesecker D., Combs L., Crown M., Kunches J. Doggett K., Singer H., and Zezula D. Halloween space weather storms of 2003. *NOAA Technical Memorandum OAR, SEC-88*, 2004.
- [4] J. M. Picone, A. E. Hedin, D. P. Drob, and A. C. Aikin. NRLMSISE-00 empirical model of the atmosphere: Statistical comparisons and scientific issues. *Journal of Geophysical Research: Space Physics*, 107(A12):SIA 15–1–SIA 15–16, 2002.
- [5] Bruce Bowman, W Kent Tobiska, Frank Marcos, Cheryl Huang, Chin Lin, and William Burke. A new empirical thermospheric density model jb2008 using new solar and geomagnetic indices. In *AIAA/AAS astrodynamics specialist conference and exhibit*, page 6438, 2008.
- [6] Bruinsma, Sean. The DTM-2013 thermosphere model. *J. Space Weather Space Clim.*, 5:A1, 2015.
- [7] Aaron Ridley, Yue Deng, and G. Tóth. The global ionosphere-thermosphere model. *Journal of Atmospheric and Solar-Terrestrial Physics*, 68:839–864, 05 2006.
- [8] Tim Fuller-Rowell et al. Transition of wam-ipe to noaa operations: Current capabilities and future potential. *17th Conference on Space Weather*, 2020.
- [9] Liying Qian, Alan G. Burns, Barbara A. Emery, Benjamin Foster, Gang Lu, Astrid Maute, Arthur D. Richmond, Raymond G. Roble, Stanley C. Solomon, and Wenbin Wang. *The NCAR TIE-GCM*, chapter 7, pages 73–83. American Geophysical Union (AGU), 2014.
- [10] Piyush M. Mehta and Richard Linares. A methodology for reduced order modeling and calibration of the upper atmosphere. *Space Weather*, 15(10):1270–1287, 2017.
- [11] David J. Gondelach and Richard Linares. Real-Time Thermospheric Density Estimation via Two-Line Element Data Assimilation. *Space Weather*, 18(2):e2019SW002356, 2020.
- [12] David J. Gondelach and Richard Linares. Real-Time Thermospheric Density Estimation via Radar and GPS Tracking Data Assimilation. *Space Weather*, 19(4):e2020SW002620, 2021.

- [13] Piyush M. Mehta, Richard Linares, and Eric K. Sutton. A quasi-physical dynamic reduced order model for thermospheric mass density via hermitian space-dynamic mode decomposition. *Space Weather*, 16(5):569–588, 2018.
- [14] Turner H., Zhang M., D. Gondelach, , and R. Linares. *Machine Learning Algorithms for Improved Thermospheric Density Modeling*, volume 12312. Springer, Cham, 2020.
- [15] National research council, continuing kepler’s quest: Assessing air force space command’s astrodynamics standards. *National Academies Press*, 2012.
- [16] David J. Gondelach, Roberto Armellin, and Aleksander A. Lidtke. Ballistic Coefficient Estimation for Reentry Prediction of Rocket Bodies in Eccentric Orbits Based on TLE Data. *Mathematical Problems in Engineering*, 2017:7309637, Dec 2017. Publisher: Hindawi.
- [17] David Gondelach, Aleksander Lidtke, Roberto Armellin, Camilla Colombo, Quirin Funke, and Tim Flohrer. Re-entry prediction of spent rocket bodies in GTO. Feb 2016. In 26th AAS/AIAA Space Flight Mechanics Meeting.
- [18] David A. Vallado. *Fundamentals of Astrodynamics and Applications*, chapter 8.6.2 Atmospheric Drag, pages 551–555. Microcosm Press, 4 edition, 2013.
- [19] J. Geul, E. Mooij, and R. Noomen. Analysis of uncertainties and modeling in short-term reentry predictions. *Journal of Guidance, Control, and Dynamics*, 41(6):1276–1289, 2018.
- [20] Sergey Ioffe and Christian Szegedy. Batch normalization: Accelerating deep network training by reducing internal covariate shift. *Proceedings of the 32nd International Conference on Machine Learning*, PMLR 37:448–456, 2015.
- [21] R. A. DeCarlo. *Linear systems: A state variable approach with numerical implementation*. Upper Saddle River, NJ, USA: Prentice-Hall, Inc, 1989.
- [22] E. A. Wan and R. Van Der Merwe. *The unscented Kalman filter*, page 221–280. New York: John Wiley & Sons, Inc., 2001.
- [23] Alessandro Morselli, Roberto Armellin, Pierluigi Di Lizia, and Franco Bernelli Zazzera. A high order method for orbital conjunctions analysis: Sensitivity to initial uncertainties. *Advances in Space Research*, 53(3), 2014.
- [24] Celestrak orbit visualization. <https://celestrak.org/cesium/orbit-viz.php?tle=/pub/TLE/catalog.txt&satcat=/pub/satcat.txt&referenceFrame=1>. Accessed: 2022-08-11.
- [25] Hiroki UTO, Toshinori KUWAHARA, and Tomoyuki Honda. Orbit verification results of the de-orbit mechanism demonstration cubesat freedom. *TRANSACTIONS OF THE JAPAN SOCIETY FOR AERONAUTICAL AND SPACE SCIENCES, AEROSPACE TECHNOLOGY JAPAN*, 17, 01 2019.
- [26] Akihisa Hattori and Toshimichi Otsubo. Time-varying solar radiation pressure on ajisai in comparison with lageos satellites. *Advances in Space Research*, 63(1):63–72, 2019.
- [27] Kent W. Tobiska, Bruce R. Bowman, and David Bouwer, editors. *COSPAR International Reference Atmosphere*, chapter Chapter 4: Solar and Geomagnetic Indices for Thermospheric Density Models. 2012. Accessed: 2022-07-05.
- [28] William Dean Pesnell. Predictions of solar cycle 24: How are we doing? *Space Weather*, 14(1):10–21, 2016.
- [29] National Weather Service. Hello solar cycle 25, 09 2020.

APPENDIX A

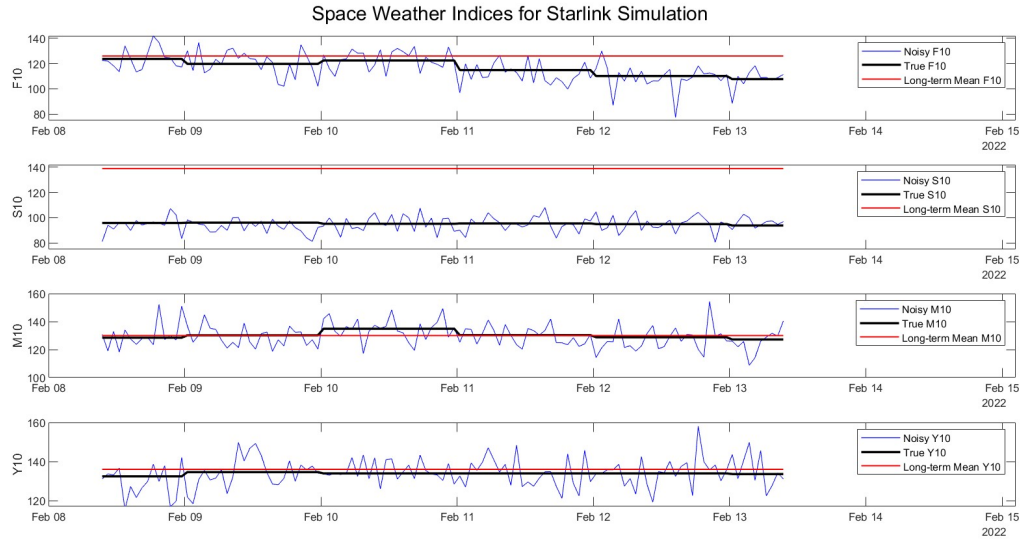


Fig. 11: True, noisy, and reference space weather values (F10, S10, M10, and Y10) for the Starlink 51470 simulation. Note that this plot represents space weather inputs for the ROM models, but not the inputs for the JB2008 model, which uses space weather data with a 1- to 5-day lag. For an explanation of noise used in JB2008, see Section 3.4.

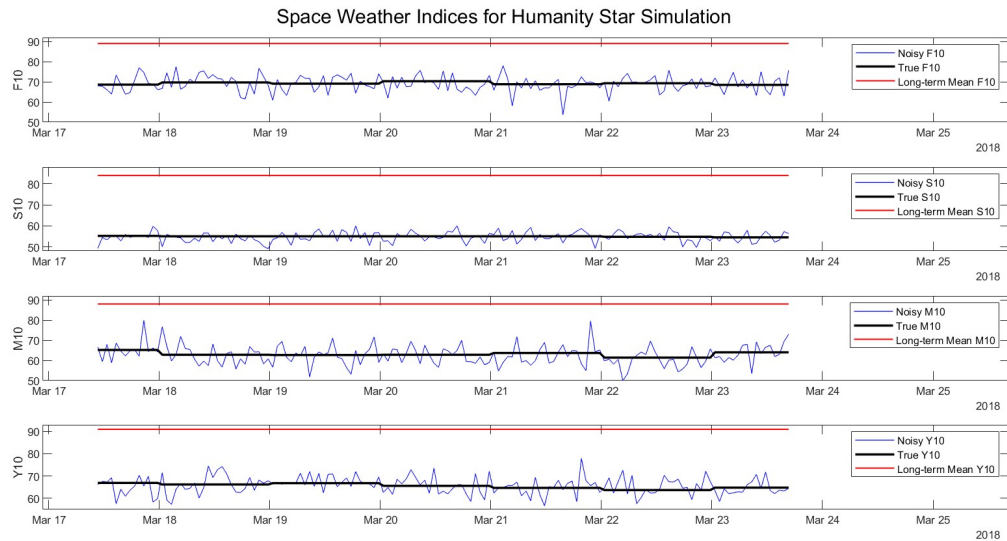


Fig. 12: True, noisy, and reference space weather values (F10, S10, M10, and Y10) for the Humanity Star simulation. Note that this plot represents space weather inputs for the ROM models, but not the inputs for the JB2008 model, which uses space weather data with a 1- to 5-day lag. For an explanation of noise used in JB2008, see Section 3.4.

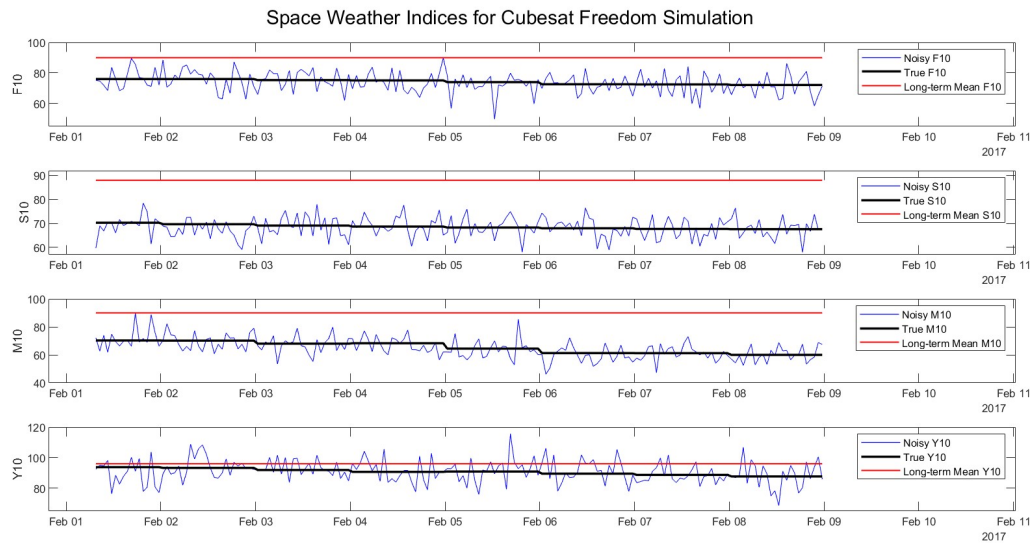


Fig. 13: True, noisy, and reference space weather values (F10, S10, M10, and Y10) for the Cubesat Freedom simulation. Note that this plot represents space weather inputs for the ROM models, but not the inputs for the JB2008 model, which uses space weather data with a 1- to 5-day lag. For an explanation of noise used in JB2008, see Section 3.4.